

Lattice Boltzmann simulation and analysis of the turbulent wake of a MAV hovering near the ground

Nicolas Gourdain[†], Deepali Singh[§], Thierry Jardin[‡] and Sébastien Prothin[‡]

Mail to: nicolas.gourdain@isae.fr

[†]Professor, Dpt. of aerodynamics, energetics and propulsion, ISAE Sup'Aero, University of Toulouse, France

[§]Master degree's student, ISAE Sup'Aero, University of Toulouse, France

[‡]Researcher, Dpt. of aerodynamics, energetics and propulsion, ISAE Sup'Aero, University of Toulouse, France

ABSTRACT

This work reports the investigations done to assess the capability of a Lattice-Boltzmann method to predict the turbulent wake of a Micro Air Vehicle rotor interacting with the ground, one diameter away from the rotor. Two configurations are investigated: a free rotor and a shrouded rotor. The Reynolds number based on the diameter and induced velocity is 0.75×10^5 . Several grid resolutions are tested, up to 830×10^6 cells. The comparison of LBM results with RANS predictions and measurements demonstrates that LBM has a good potential to predict the turbulent flow in this configuration, both regarding mean velocity and turbulent flow fields.

Abbreviation and symbols

LES	Large Eddy Simulation	
LBM	Lattice Boltzmann Method	
MAV	Micro Air Vehicle	
RANS	Reynolds-Averaged Navier-Stokes	
TKE	Turbulent Kinetic Energy	
C_T	Thrust coefficient, Eq. (5)	[-]
k	Turbulent kinetic energy	$[m^2 \cdot s^{-2}]$
P_{ij}	Turbulence production terms	$[m^2 \cdot s^{-3}]$
ω	Rotational speed	$[rad \cdot s^{-1}]$
x / r	Radial position	[m]
R	Rotor radius	[m]
v_z, v_θ, v_r	Streamwise, tangential and radial velocity components	$[m \cdot s^{-1}]$
z	Distance to the ground	[m]

sandy landing area. The main difficulties to accurately predict the interaction between the rotor and the ground are related to the relative motion between the blades and the ground, 3D flow effects and turbulence.

Analytical models can provide useful information about the aerodynamic performance of the rotor operating in ground effect (Khromov and Rand, 2008). However, a better description of the flow, including turbulence, requires to consider experimental facilities (Ganesh and Komerath, 2004; Lee *et al.*, 2008) or numerical simulations. The most popular method to simulate such rotor/ground interaction is the Reynolds Averaged Navier-Stokes (RANS) approach. The capability of numerical simulations to predict the flow for such problems imposes to properly resolve the wake generated by the rotor (especially the tip vortex) down to the ground (Kalra *et al.*, 2011). Classical RANS models require assumptions about turbulence that are not validated in such geometries. With the increase in computing power, Large Eddy Simulation (LES) emerges as a promising technique to improve both knowledge of complex physics and reliability of flow solver predictions (Wu and Piomelli, 2016). Unfortunately, the computing cost and the difficulty to represent the real geometry still limit its applicability to industrial problems. In that regard, the use of a Lattice-Boltzmann based flow solver can help to overcome these difficulties. However, due to their recent emergence, this numerical approach suffers from a lack of validation.

1. INTRODUCTION

Micro air vehicles (MAVs) can operate in highly confined environments, for example for civil rescue missions or archaeology investigations. In these confined environments, the distance between the rotor and the ground is reduced, resulting in a ground effect that affects the rotor performance (Sugiura *et al.*, 2015). Such ground effects are known to modify the lift, induce undesirable flow unsteadiness and can be responsible for maneuverability problems, for example in the case of a helicopter in hover flight above a

This work reports the investigations done to assess the capability of such a Lattice-Boltzmann method (LBM) to deal with the turbulent flow around a MAV rotor interacting with the ground. The main objective is to study the turbulence generated by the interaction between the rotor wake and the ground. MAVs operate at Reynolds numbers ranging from 10^4 to 10^5 and at low Mach numbers ($M \sim 0.1$). Since the cost of LES scales with the Reynolds number, MAVs are particularly well-suited configurations.

This paper is organized in four parts. First, the configuration and the numerical method are described. The Lattice-Boltzmann Method is briefly presented, as well as the boundary conditions and numerical parameters. Then, numerical predictions based on RANS and LBM are compared to experimental measurements. A particular care is brought to the validation of results at the ground level and in the rotor wake, through comparison of velocity profiles and turbulent kinetic energy profiles. Then, a comparison of the turbulent flow is done between a free rotor and a shrouded rotor.

2. CONFIGURATION AND METHOD

2.1 Experimental facility and measurements

The experimental facility is shown in Fig. 1. The facility is designed specifically to study the interaction of the rotor with walls. In the present case, only the bottom wall is considered to model the ground. The rotor is located at a distance of two radius from the ground, $h/R=2.0$ (with R the rotor radius). A mechanical traverse is used to adjust the rotor-to-wall distance. The rotor is in hover flight (the velocity far from the rotor is 0 m.s^{-1}).

The main parameters of the configuration are sum-up in Table 1. The rotor is composed of two untwisted flat plates, with a radius $R=0.125\text{m}$. The chord of the blade C is 0.025m (*i.e.* $C=R/5$) and the distance between the roots of the two blades is two chords. The blades have a constant pitch angle, $\theta=15^\circ$. The rotation speed of the rotor is set to $3,960 \text{ rpm}$, which corresponds to a tip speed $V_{\text{tip}} = \omega \cdot R = 51.84 \text{ m.s}^{-1}$.

The flow close to the rotor walls is characterized by a Reynolds number based on the rotation speed and the chord C , $Re_{\text{rotor}}=86,000$. However, the characterization of the interaction between the rotor flow and the ground is better related to a Reynolds number based on the rotor diameter $2 \cdot R$ and the induced speed V_i ,

which is linked to the rotor thrust T as

$$(1) \quad V_i = \sqrt{T / (2\pi\rho \cdot R^2)}$$

Based on these parameters, the Reynolds number is $Re_{\text{ground}}=74,900$.

The rotor is powered by a AXI 2808/24 goldline brushless motor. The experimental data relies on the Particle Image Velocimetry (PIV) technique. The PIV system consists of a $2 \times 200 \text{ mJ}$ DualPower Bernoulli laser to which two FlowSense EO 16M cameras are synchronized, using DantecStudio commercial software. PIV images are acquired at a normalized frequency $f^* = f / [2\pi/\omega] = 0.038$. The PIV resolution is $\Delta/R=0.002$. Time-averaged flow fields are evaluated by means of 1,000 samples, to ensure the convergence of statistics. More details about measurements can be found in Jardin *et al.* (2015).

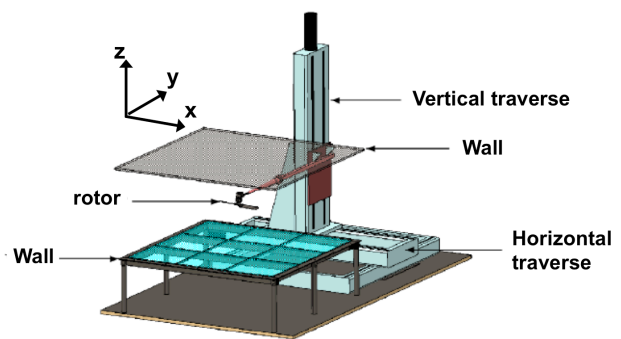


Fig. 1 Overview of the experimental facility to study the ground effect (Jardin *et al.*, 2015a)

The data presented in this paper consider a standard atmosphere, with temperature $T=288\text{K}$ and pressure $p=101325\text{Pa}$.

Table 1. Parameters of the configuration

Rotation speed, ω	3,960 rpm
Rotor radius, R	0.125m
Rotor chord, C	$R/5$
Reynolds, based on radius and induced speed, Re	0.75×10^5
Pitch angle, θ	15°
Rotor to ground distance, h	$2.0R$

2.2 Lattice-Boltzmann approach

The governing equations of the lattice Boltzmann method consider the probability $f_i(x,t)$ to have a set of particles at location x and time t , with a velocity c_i (Lallemand and Luo, 2000; D'humieres *et al.*, 2002):

$$(2) \quad f_i(x + c_i \delta t, t + \delta t) = f_i(x, t) + \Omega_{ij}(x, t),$$

for $[0 < i, j < N]$, where c_i is a discrete set of N velocities and Ω_{ij} is an operator representing the internal collisions of pairs of particles. For 3D problems, a common choice for the set of velocities is the D_3Q_{19} scheme (19 velocities, so Eq. (2) is solved 19 times, for each velocity c_i). This kinetic scheme ensures the conservation of mass and momentum, which are related to the population of f_i as

$$\rho = \sum_{i=1}^N f_i \quad \rho \mathbf{u} = \sum_{i=1}^N f_i \mathbf{c}_i$$

The collision operator Ω_{ij} is modeled with the BGK approximation (Bhatnagar *et al.*, 1954), which consists in a relaxation of every population towards its equilibrium state f_i^{eq} :

$$(3) \quad \Omega_{ij} = -\frac{1}{\tau} [f_i(x, t) - f_i^{(eq)}(x, t)]$$

The operator collision is related to the kinematic viscosity ν (and thus to the Reynolds number) through the relaxation parameter τ as

$$\nu = c_s^2 \left(\tau - \frac{1}{2} \right),$$

with c_s the pseudo-sound speed ($c_s = 1/\sqrt{3}$ for the kinetic scheme D_3Q_{19}). As for the Navier-Stokes equations, the effects of turbulence can be modeled through the Boussinesq approximation by modifying the effective value of the viscosity ν .

The LBM equations, Eq. (2), are solved using the open source software Palabos (www.Palabos.org), developed by the University of Geneva. The Palabos library is a framework for general-purpose CFD with a kernel written in C++. The numerical method is divided into two steps:

- A collision phase, which can be written as

$$f_i(x, t + \frac{1}{2}) = f_i(x, t) + \frac{1}{\tau} [f_i^{(eq)}(\rho, \mathbf{u}) - f_i(x, t)],$$

where the equilibrium function f_i^{eq} is computed using the physical values at time t ,

- A stream phase, where the new functions f_i are transported to the adjacent lattices, as

$$f_i(x + c_i, t + 1) = f_i(x, t + \frac{1}{2}).$$

To reduce the cost of the calculations compared to DNS, the numerical simulation relies on a Large-Eddy Simulation (LES), with the Smagorinsky model (the constant C_S is set to 0.18). More information about subgrid scale models for LBM can be found in Malaspina and Sagaut (2012). To model the effects of turbulence near the walls, a wall model is used, based on the approach proposed by Wang and Moin (2002).

2.3 Boundary conditions and domain

LBM requires the use of Cartesian grids ($\Delta x = \Delta y = \Delta z$). To account for the presence of walls, it relies on the use of an immersed boundary (IB) method, well suited to complex geometries, as well as moving bodies (Ota *et al.*, 2012). This method allows computing the intersection between the geometry and the Cartesian grid, by means of an iterative process (Inamuro, 2012). The boundary condition corresponding to the moving (rotating) walls is thus applied at different lattices at each time step.

The numerical domain is represented in Fig. 2. Outlet boundary conditions (with uniform pressure) are applied on all lateral faces and an inlet velocity condition is imposed on the top face. The ground is located at the bottom face.

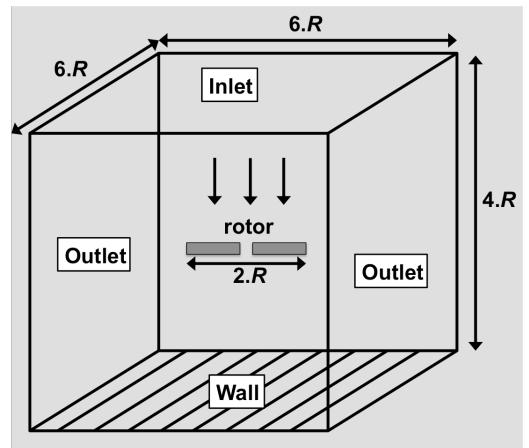


Fig. 2 Numerical domain and boundary conditions

All boundary conditions, except the wall, are

associated with sponge layers with a thickness of $R/2$ to avoid the reflection of pressure waves and damp turbulence before it reaches the boundary condition.

A Cartesian grid is used in this work, without grid refinement. The consequence is that the cost of the simulation is proportional to the volume of the box. A RANS-based simulation has been first performed, to identify the minimum size of the domain to avoid the influence of boundary conditions on the pressure field.

The compromise adopted is to use a $6R \times 6R \times 4R$ domain. Fig. 3 shows the pressure coefficient, defined as

$$(4) \quad C_p = \frac{(p - p_\infty)}{1/2 \times \rho(\omega \cdot R)^2},$$

on a slice at the center of the domain. The pressure field is not affected in the vicinity of the rotor and the flow is correctly driven outside the domain. The flow field in Fig. 3 also indicates that the pressure coefficient is small compared to the rotor velocity, which explains why this small volume is sufficient to limit the influence of boundary conditions on the pressure field.

To obtain a statistically converged flow field, the simulation is run for 30 rotor rotations. Then, 720 samples are used to estimate the flow statistics. These samples are extracted at four angular position, with an angular step $\Delta\theta=2\pi/4$, and with a time period $\Delta t=[2.\pi/\omega]/11$ (i.e. 11 samples per rotation).

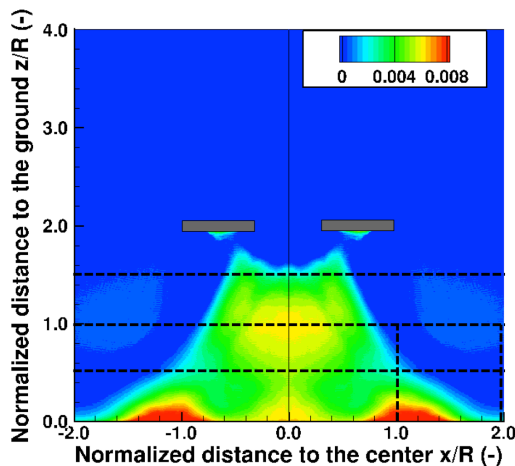


Fig. 3 Time-averaged pressure coefficient, $C_p=(p-p_\infty)/[1/2.\rho(\omega.R)^2]$, $6R \times 6R \times 4R$ domain (dashed lines indicate the sections used for analysis)

2.4 RANS approach

To compare with the data provided by LBM, unsteady RANS calculations are performed at the same operating conditions (Table 1). The Navier-Stokes equations are solved using the commercial CFD software STAR-CCM+. The numerical scheme is a 2nd order centered scheme. An implicit unsteady solver is used with a time step corresponding to 1 degree of rotation (so one rotation is discretized by 360 time steps). The turbulence is modeled with a two-transport equations $k-\epsilon$ model.

To reduce the complexity of the grid, only the two blades are simulated, without the motor, so a gap between the two blades is present in the numerical simulations. A 3D unstructured grid with polyhedral cells is used to mesh the geometry, with a prism layer for the boundary layers around the rotor blades. A grid is associated to the rotor and its rotation in the rest of the grid is done thanks to an overset grid method. The mean normalized distance to the wall is set to $y^+ \sim 1$ and the total number of grid points is 3×10^6 . A grid convergence study has been achieved to ensure that the time-averaged flow field does not depend on the grid density.

2.5 Computational cost

For unsteady RANS simulations, the calculation is run for 30 rotations to achieve a periodic flow. The computational cost is about 2,000 CPU hours (each simulation is run on 16 cores of a scalar computer). The mean code performance is $200 \mu s/\Delta t/\text{point}$.

For LBM, three mesh resolutions are tested, as shown in Table 2. For each grid, the grid resolution is increased by a factor 2, compared to the previous grid. For stability reasons, the time step is also divided by a factor 2 when moving from one grid level to the other. For the finest grid (grid 3), the time step corresponds to 0.03 degree (so one rotation is discretized by 12,000 time steps). For grid 3, the total CPU cost to achieve 30 rotations of the rotor is 180,000 hours. The code performance is estimated at $2 \mu s/\Delta t/\text{point}$ (including the extraction of data).

Table 2. Grid resolution for LBM and CPU cost

	Resolution, $R/\Delta x$	Grid points	CPU hours (h)
LBM – grid 1	48 ($y^+ \sim 200$)	13×10^6	600
LBM – grid 2	95 ($y^+ \sim 100$)	105×10^6	11,000
LBM – grid 3	190 ($y^+ \sim 50$)	830×10^6	200,000

The parallel performance of the LBM code is shown in Fig. 4 on a classical scalar computer (for grid 3). The speed-up is normalized by the performance on 100 cores, which is the minimum number of cores for memory cost limitations. Benchmarks have been performed up to 1,600 cores, showing a parallel efficiency of 85%.

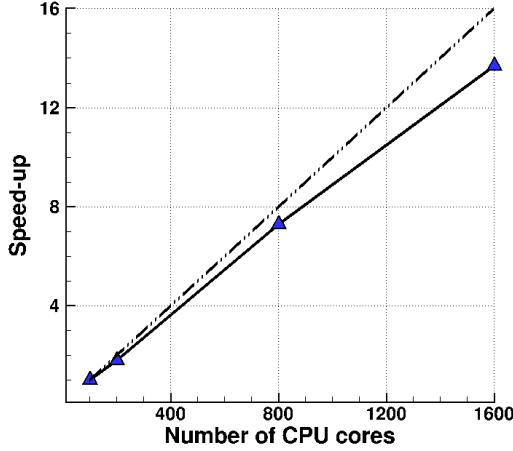


Fig. 4 Parallel performance (speed-up) of the LBM solver on a scalar computer. The speed-up is normalized by the performance on 100 cores.

3. COMPARISON WITH EXPERIMENTAL DATA

3.1 Prediction of thrust and velocity

The prediction of thrust is of paramount importance since it is linked to the induced velocity V_i , Eq. (1), which is a driving parameter for the interaction between the rotor flow and the ground. The data obtained with RANS and LBM are used to estimate the thrust coefficient of the rotor, defined as

$$(5) \quad C_T = \frac{T}{\frac{1}{2}\rho(\omega \cdot R)^2 \cdot (\pi R^2)}$$

The values of the thrust coefficient are reported in Table 3. Unsteady RANS under-predicts the value of C_T by 11%, compared to measurements. Due to the use of a Cartesian grid, LBM results are very sensitive to the grid resolution, since the discrepancy on grid 1, grid 2 and grid 3 are 33%, 14% and 10%, respectively. The main reason to explain the discrepancy between RANS, LBM and measurements comes from the recirculation flow at the center of the rotor that is present only in the numerical simulations (due to the lack of the motor).

The effect of the rotor is highlighted on Fig. 5 that shows the velocity signals at two different distance to the ground, $z/R=1.0$ and $z/R=1.5$.

Table 3. Estimation of the thrust coefficient C_T

	Thrust coefficient C_T
Experimental data	0.035
Unsteady RANS	0.032
LBM – grid 1	0.024
LBM – grid 2	0.030
LBM – grid 3	0.032

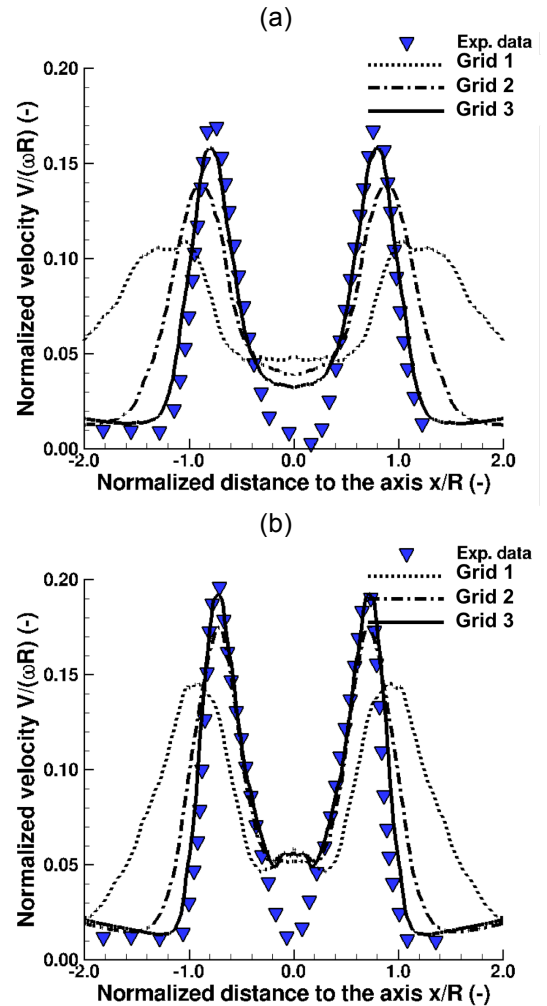


Fig. 5 Time-averaged normalized velocity: (a) $z/R=1.0$ and (b) $z/R=1.50$.

RANS results are not shown for clarity reasons, but the velocity signals predicted with RANS are very close to those predicted with LBM on grid 3.

At $z/R=1.5$, close to the rotor, LBM on grid 1 and grid 2 under-predicts the peak velocity by 25% and 8%, respectively. Only LBM on grid 3 successfully predicts the peak velocity. As for the thrust coefficient, the discrepancy with measurements, close to the rotation axis ($x/R=0.0$), is related to the motor withdraw in the numerical simulations. At $z/R=1.0$, approaching the ground, LBM on grid 1, grid 2 and grid 3 under-predicts the peak velocity by 38%, 20% and 7%, respectively. The thickness of the rotor wake is well predicted by LBM on grid 3, even far from the rotor.

The decrease in the accuracy of LBM predictions when approaching the ground is related to the difficulty to predict the mixing between the rotor flow and the main flow. In that regards, the capability to predict the turbulent kinetic energy is of paramount importance. Only data obtained with RANS and LBM on grid 3 are analyzed in the rest of the paper.

3.2 Production of turbulence

The turbulent kinetic energy (TKE), defined as

$$(6) \quad k = \frac{1}{2} \overline{u_i u_i}$$

is presented in Fig. 6 to compare RANS and LBM results with measurements.

It is worth to mention that in the present case, TKE also contains a part of fluctuations related to the periodic motion of the rotor. To ensure a fair comparison with measurements, these periodic fluctuations have been added in the unsteady RANS data and are not filtered in LBM data.

RANS and LBM predictions are in good agreement with measurements. TKE is mainly observed in the vicinity of the rotor, close to the rotor tip, due to the tip vortex and its interaction with the rotor wake, as observed in Fig. 7. LBM shows a massive flow separation at the rotor leading edge, which is responsible for an important blade-to-blade interaction.

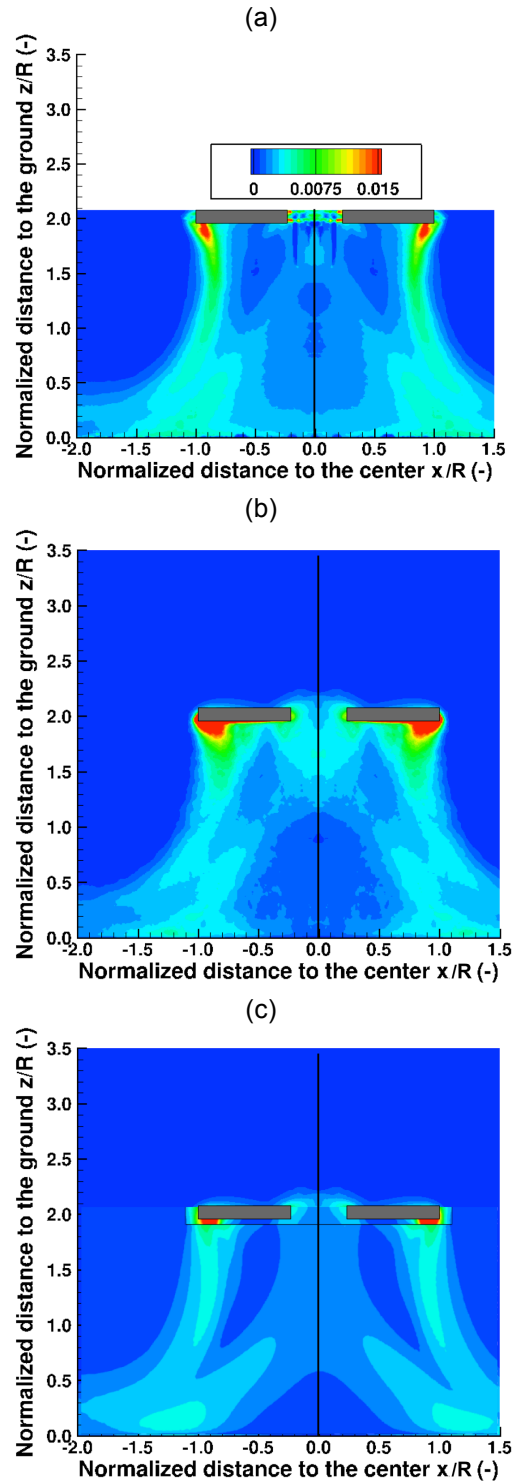


Fig. 6 Normalized TKE, $2.k/(\omega R)^2$: (a) experimental data, (b) LBM (grid 3) and (c) unsteady RANS.

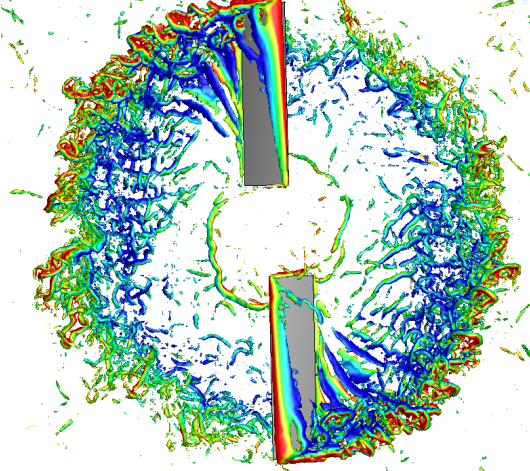


Fig. 7 Instantaneous Q criterion around the rotor, colored with velocity V_z (blue: velocity directed towards the ground, red: velocity directed towards the top). Data from LBM on grid 3.

The result of this intense leading edge vortex is that LBM over-estimates the azimuthal velocity V_θ , close to the rotor, compared to measurements, Fig. 8. Close to the ground, this discrepancy disappears and LBM correctly predict the azimuthal velocity V_θ .

The contraction of the wake below the rotor is well highlighted in Fig. 6. This well-known effect is related to the mass conservation (Froude theory). This wake contraction induces a radial velocity directed towards the rotation axis, which counter-balances the centrifugal forces due to the flow rotation. In the present case, RANS, LBM and experiments show that TKE is mainly produced in the external part of the rotor wake. For example, at $z/R=1.0$, the region of turbulent activity spreads from $x/R=\pm 0.8$ to $x/R=\pm 1.1$ while the rotor wake extends from $x/R=\pm 0.4$ to $x/R=\pm 1.2$ (see Fig. 5).

Close to the ground ($z/R < 0.5$, $x/R = 1.0$), a region of intense TKE develops, due to the interaction between the rotor wake and the ground. RANS underestimates the value of TKE in this area, but LBM shows a good agreement with experimental data, both regarding the intensity of the TKE and the location where it is produced.

To explain the shape of the TKE field, it is necessary to quantify the production terms of turbulence, which are related to the velocity gradients, as

$$(7) \quad P_{ij} = -\rho \overline{v_i v_j} \frac{\partial V_i}{\partial x_j}$$

For axisymmetric flows (as in the present case), the derivative terms vanish in the azimuthal direction, θ .

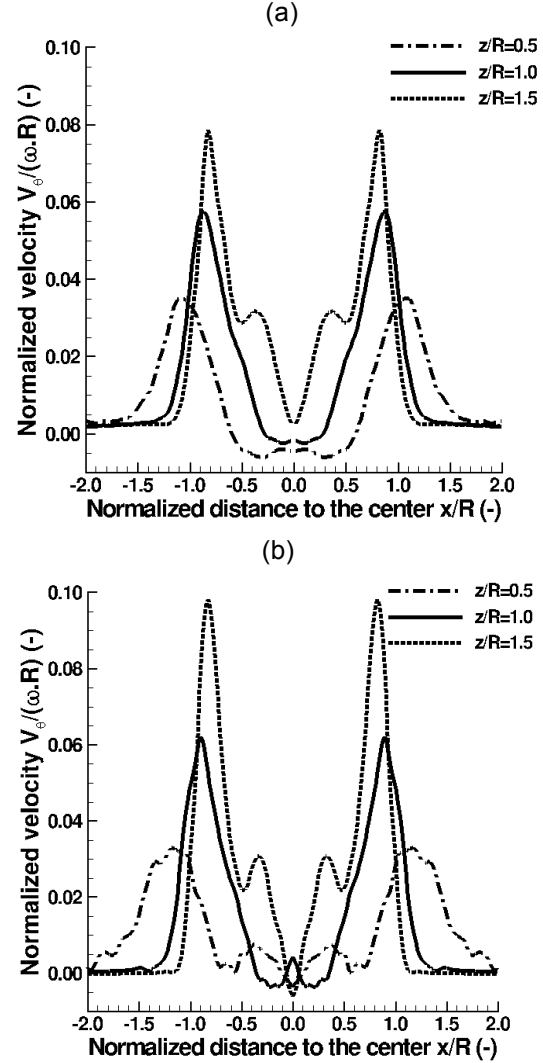


Fig. 8 Time-averaged azimuthal velocity: (a) measurement and (b) LBM (grid 3).

In cylindrical coordinates, the production terms for v_z , v_θ and v_r are thus given by

$$(8) \quad P v_z / \rho = -\overline{v_z \cdot v_z} \frac{\partial V_z}{\partial z} - \overline{v_z \cdot v_r} \frac{\partial V_z}{\partial r}$$

$$(9) \quad P v_\theta / \rho = -\overline{v_\theta \cdot v_z} \frac{\partial V_\theta}{\partial z} - \overline{v_\theta \cdot v_r} \frac{\partial V_\theta}{\partial r}$$

$$(10) \quad P v_r / \rho = -\overline{v_r \cdot v_z} \frac{\partial V_r}{\partial z} - \overline{v_r \cdot v_r} \frac{\partial V_r}{\partial r}$$

As a first approximation, far to the ground, the derivatives in the z -direction can be neglected. The production of turbulence is thus mainly supported by

the gradients in the radial direction. The velocity gradients are more important in the external part of the rotor wake, along the trajectory of the tip vortex, Fig. 5, which explains why TKE is mainly observed in this region.

When approaching the ground, the derivative terms in the z-direction can no longer be neglected, since the flow changes its trajectory from the z-direction to the radial direction r . Indeed, the production of turbulence should move from the external part of the rotor wake towards the internal part, where the negative gradient is maximal due to the ground blockage effect. Once the rotor wake has impacted the ground, the flow is ejected towards the outside of the domain and a classical boundary layer develops.

The total production term is represented in Fig. 9, to compare LBM predictions with experimental data.

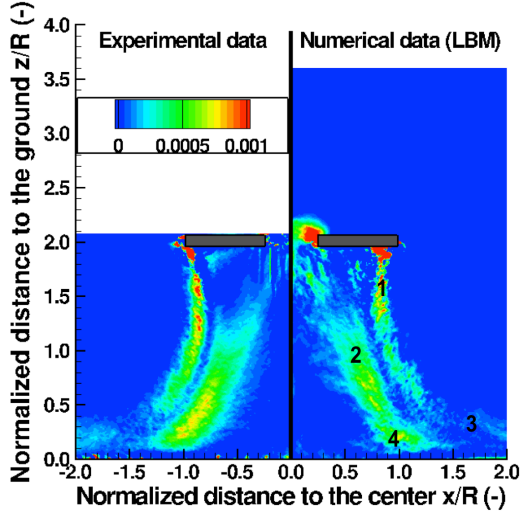


Fig. 9 Normalized production term $P_t/[(\omega R)^3] \cdot R$. Comparison between measurements (left) and LBM (right)

Both sets of data are in very good agreement. In the vicinity of the rotor, the external part of the rotor wake is well responsible for the production of turbulence (1). Both LBM and measurements show that this region has the strongest effect on the production of turbulence, in this configuration. When approaching the ground, the velocity decreases in the z-direction, resulting in a new zone of turbulence production (2). After the flow direction has turned to the radial direction, turbulence is produced in the boundary layer (3). Measurements and LBM also indicate an important production of turbulence at the point where the rotor wake hits the ground (4), which is located at $x/R=1.0$ in both cases.

3.3 Effect of rotation on turbulence

The rotation of the flow does not contribute directly to the production of turbulence. However, rotation acts on the Reynolds shear stress, which in turn affects the production terms, Eq. (8-10). In the present case, the z-direction is aligned with the vector rotation, so the influence on the component v_z is negligible and rotation will redistribute energy among v_r and v_θ components, through the rotation terms

$$F_{v_\theta} = -4\rho \frac{V_\theta}{r} \overline{v_\theta \cdot v_r},$$

$$F_{v_r} = +4\rho \frac{V_\theta}{r} \overline{v_\theta \cdot v_r}.$$

The rotation will also affect the shear stress component $v_\theta \cdot v_r$, through (Gundersen, 2011)

$$(11) \quad F_{v_\theta v_r} = -2\rho \times \frac{V_\theta}{r} \cdot (\overline{v_r^2} - \overline{v_\theta^2})$$

For $v_r^2 > v_\theta^2$, the Reynolds shear stress $[v_\theta \cdot v_r]$ is decreased by the effect of rotation. In the external part of the rotor wake, the Reynolds shear stress $[v_\theta \cdot v_r]$ is positive. Rotation will thus decrease the fluctuations of V_θ and increase those on V_r . In the internal part $[v_\theta \cdot v_r]$ is negative, so rotation will act in the opposite way.

The value of the rotation term $F_{v_\theta v_r}$, Eq. (11), is shown in Fig. 10. The regions colored in red correspond to a positive contribution of rotation to the shear stress $[v_\theta \cdot v_r]$ (where $v_r^2 < v_\theta^2$). The contribution of rotation to turbulence is one order of magnitude below the contribution of the direct production terms.

In the vicinity of the rotor (noted 1 in Fig. 10), measurements and LBM show opposite effects: LBM predicts a positive contribution of rotation to the shear stress $[v_\theta \cdot v_r]$, while measurements shows a negative one. As previously mentioned, the over-prediction of V_θ close to the rotor tip in LBM is responsible for the larger production of turbulence on the θ component.

At the end of the wake contraction (2), the fluctuations of the v_θ component overtake the fluctuations of the v_r component, also in the measurements (and so the contribution of rotation to the shear stress $[v_\theta \cdot v_r]$ becomes positive). Below $z/R=1.0$ (3), both measurements and LBM show that rotation has a negative effect on the shear stress $[v_\theta \cdot v_r]$ and will transfer energy from the θ -component to the r -

component. Very close to the ground (4), at $x/R=1.0$, a positive contribution of the rotation term is also highlighted, corresponding to the point where a part of the rotor wake is directed towards the rotation axis.

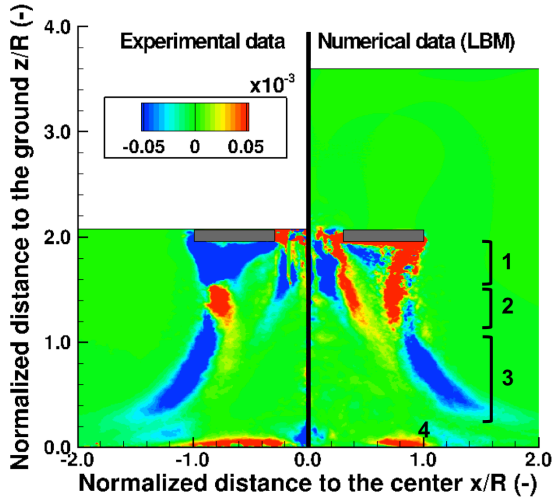


Fig. 10 Normalized rotation term $F_{v\theta, vr}/[(\omega R)^3].R$. Comparison between measurements (left) and LBM (right)

3.4 Boundary layers at the ground

The interaction of the rotor wake with the ground is responsible for the development of a boundary layer directed towards the outlet of the domain. The velocity magnitude and turbulent kinetic energy are shown in Fig. 11 at two locations, $x/R=1.0$ (where the rotor wake impacts the ground) and $x/R=2.0$. LBM and measurements are in good agreement for the velocity profiles, Fig. 11(a). At $x/R=1.0$, the shape of the velocity profile is driven by the shear layer of the rotor wake. LBM under-predicts the velocity at the peak by 5% and the location of the velocity peak is shifted from $z/R=0.55$ (experimental data) to $z/R=0.60$. At $x/R=2.0$, the velocity profile is driven by a mixing between the ground boundary layer and the rotor wake. The thickness of the shear layer is $0.4R$.

LBM successfully predict the shape of the TKE profiles. Profiles at $x/R=1.0$ show three peaks: 1) one peak close to the ground at $z/R=0.03$, corresponding to the ground boundary layer, 2) one peak at $z/R=0.2$ corresponding to the internal part of the rotor wake and 3) one peak at $z/R=0.8$, corresponding to the external part of the rotor wake. However, LBM underestimates the value of TKE at the peaks by 15% compared to measurements. At $x/R=2.0$, two peaks of TKE are observed: one close to the ground, at $z/R=0.03$ and the second one at $z/R=0.2$,

corresponding to the center of the shear layer generated by the rotor wake.

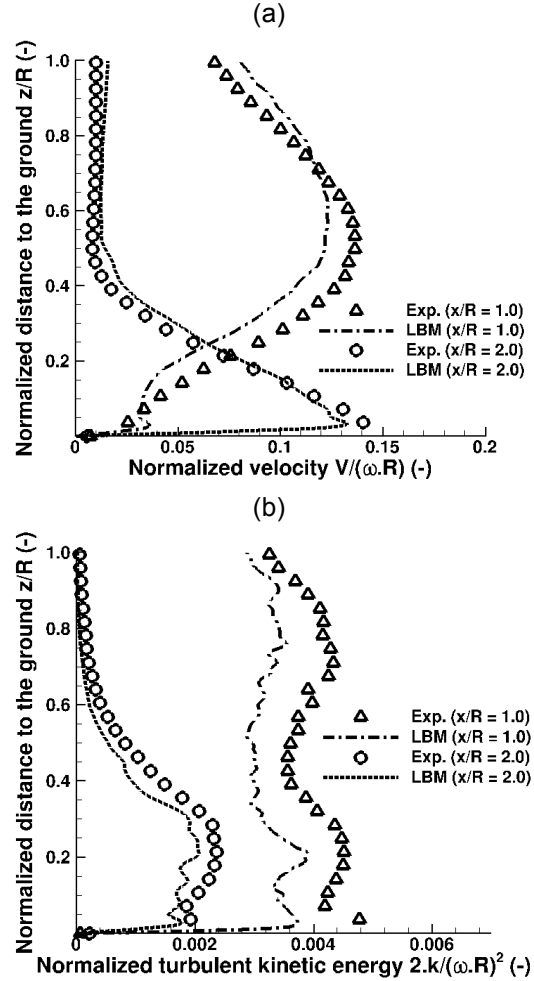


Fig. 11 Comparison of LBM data with measurements in the vicinity of the ground: (a) velocity and (b) turbulent kinetic energy

4. INFLUENCE OF A SHROUD ON THE ROTOR/GROUND INTERACTION

Shrouded rotors usually generate more thrust than equivalent free rotors (Jardin *et al.*, 2015b). Another effect of the shroud is to decrease the velocity in the diffuser, so the influence of the rotor on the ground could be reduced. The immersed boundary approach is well suited to such a case as it allows continuing LBM simulation on grid 3 by simply adding a shroud around the rotor. Twenty additional rotations of the rotor are achieved and statistics are computed in the same way than for the free rotor.

The length of the shroud is $L=1.5R$. The rotor is located at the center of the duct, where the radius is constant. The wall angle in the diffuser is set to a

constant value of 11.3° . The tip gap is $0.024R$ (so the number of grid cells inside the tip leakage is 5). More information about the design of the shroud can be found in Huo *et al.* (2015).

One of the effects of the shroud on the rotor is to replace the tip vortex by a tip leakage flow, as observed in Fig. 12. However, the separation at the rotor leading edge is still present and the negative flow at the center of the rotor is more intense.

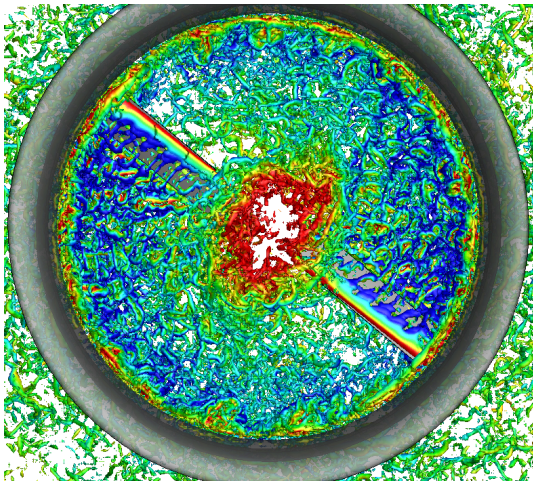


Fig. 12 Instantaneous Q criterion in the ducted rotor, colored with streamwise velocity (blue: velocity directed towards the ground, red: velocity directed towards the top). Data from LBM on grid 3.

The mean velocity flow field is shown in Fig. 13. The shroud is responsible for a shift of the location where the rotor wake impacts the ground, that moves from $x/R=1.0$ (free rotor) to $x/R=1.3$, which corresponds to the diffuser angle. The thickness of the wake is reduced by 20% and the flow is accelerated along the shroud walls, compared to the free rotor.

The influence of the shroud on the turbulent flow is shown in Fig. 14, at three locations. Close to the rotor ($z/R=1.5$), the shroud reduces the TKE peaks by 20%. The thickness of the peaks is also reduced by 50%. When moving closer to the ground ($z/R=1.0$), the peaks of TKE is increased by 30% with the shroud compared to the free rotor. This increase of the TKE is due to the shear layer that develops on the external part of the rotor wake, at the exit of the shroud. At $z/R=0.5$, the turbulent activity remains at a level 30% higher with the shroud than for the free rotor. The shape of the signals are identical with the two peaks corresponding to the internal and external shear layers of the rotor wake.

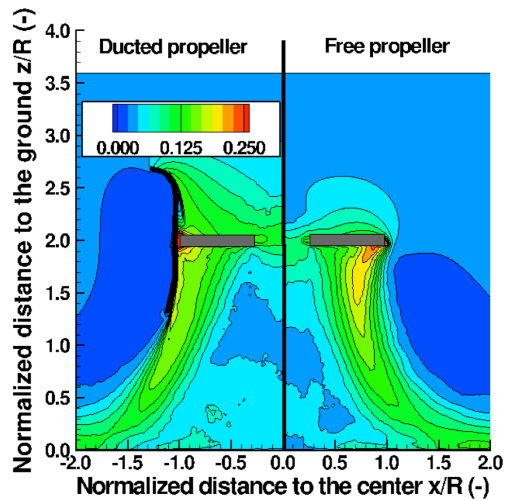


Fig. 13 Time-averaged normalized velocity field $V/(\omega R)$: ducted rotor (left) and free rotor (right)

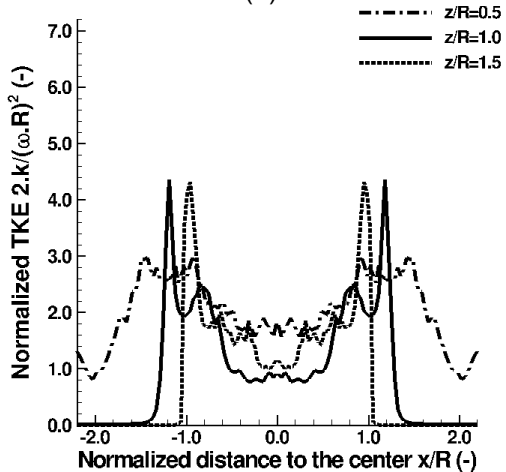
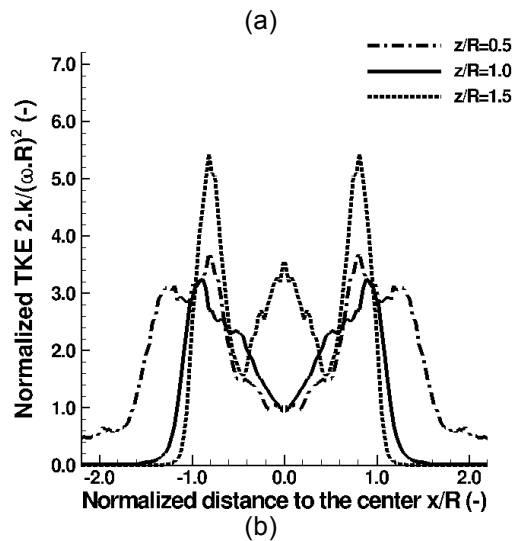


Fig. 14 Effect of the shroud on the normalized TKE $2.k/(\omega R)^2$: (a) free rotor and (b) ducted rotor

Time-averaged velocity and TKE are plotted in Fig. 15, at two radial positions $x/R=1.0$ and $x/R=2.0$. At $x/R=1.0$, the shroud is responsible for a shift of the velocity peak from $z/R=0.6$ (free rotor) to $z/R=1.0$ (shrouded rotor). As already shown in Fig. 13, the peak velocity is more important by 20% in the shrouded case. At $x/R=2.0$, the velocity profiles are close to each other, except that the presence of the shroud reduces again by 20% the peak velocity.

The effects of the shroud on turbulence close to the ground are to reduce TKE at $x/R=1.0$ (because the rotor wake has not yet impacted the ground at this location) and to increase it by 10% to 20% at the ground level (below $z/R=0.2$).

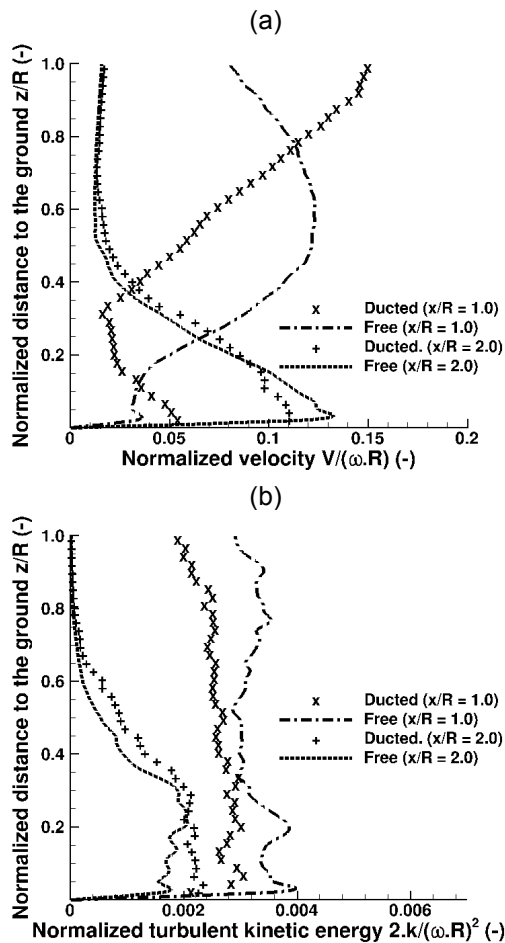


Fig. 15 Comparison of the ducted rotor with the free rotor, in the vicinity of the ground: (a) velocity and (b) turbulent kinetic energy

While such analysis provides evidence of the influence of the shroud at a given rotor rotation speed, it does not allow for a thorough comparison between rotor wakes of free and shrouded rotors at a given total

thrust, which from a practical perspective is of paramount importance. In particular, it is expected that the rotor thrust of the shrouded-rotor configuration be roughly halved, with respect to the free-rotor configuration, to provide similar total thrust. This reduction in rotor thrust will greatly reduce the resulting wake velocities and TKE.

5. CONCLUSION

This work focuses on the comparison of LBM with RANS simulations and measurements, as well as the analysis of the turbulent flow field. The configuration investigated is a two-blade rotor of a micro air vehicle (MAVs), in interaction with the ground. An attempt has also been done to reduce the rotor/ground interaction by adding a shroud to the rotor.

This works can be sum-up by the following points:

- The LBM solver shows excellent computing performance (efficiency is 85% on 1,600 cores for a computing time of $2 \mu s/\Delta t/\text{point}$).
- The comparison of results with measurements demonstrates that LBM has a good potential to predict turbulent flows, both regarding velocity and turbulence properties (including production terms). This work also shows that, similarly to LES performed with Navier-Stokes based solvers, LBM is very sensitive to the grid density.
- Turbulence in this configuration is produced in the vicinity of the rotor (tip vortex) and in the shear layer generated by the rotor wake. When approaching the ground, the slowdown of the rotor wake is also responsible for the production of turbulence. The influence of rotation on turbulence production has been quantified, showing it has an influence of one order of magnitude below the turbulence production due to the mean shear flow.
- The presence of a shroud helps to suppress the tip vortex (replaced by a tip leakage flow). However, the shroud does not affect in a significant way the flow close to the ground (the shear stress generated by the flow at the exit of the diffuser increase turbulence and counter-balances the initial reduction of turbulence due to the suppression of the rotor tip vortex), when operating at a similar rotation speed to that of a free-rotor. In that regard, future work will have to consider shrouded-rotor and free-rotor operating at similar total thrust.

The increase of the diffusion process in the shroud is a potential way to reduce the influence of the rotor on the ground. However, it requires being able to keep the boundary layer attached, which remains a challenge for high diffusion angles.

6. ACKNOWLEDGEMENT

LBM-based simulations have been performed at the computing center of the Federal University of Toulouse (CALMIP), under project p1425. The technical team of DAEP at ISAE-Supaero has been in charge of the acquisition of the experimental data. These supports are greatly acknowledged. The authors also thank the development team of Antares (<http://cerfacs.fr/antares>) at CERFACS, for providing the software used for post-processing.

Copyright Statement

The authors confirm that they, and/or their company or organization, hold copyright on all of the original material included in this paper. The authors also confirm that they have obtained permission, from the copyright holder of any third party material included in this paper, to publish it as part of their paper. The authors confirm that they give permission, or have obtained permission from the copyright holder of this paper, for the publication and distribution of this paper as part of the ERF proceedings or as individual offprints from the proceedings and for inclusion in a freely accessible webbased repository.

REFERENCES

- [1] Bhatnagar, P.L. Gross, E.P. Krook, M. (1954). A model for collision processes in gases. I. Small amplitude processes in charged and neutral one-component systems, *Phys. Rev.* 94 (3)
- [2] D'Humieres, D., Ginzburg, I. Krafczyk, M. Lallemand, P. and Luo, L. S. (2002). Multiple-relaxation-time lattice Boltzmann models in three dimensions, *Phil. Trans. R. Soc. Lond. A* 360, 437-451
- [3] Ganesh, B. and Komerath, N. (2004). Unsteady aerodynamics of rotorcraft in ground effect. *AIAA Fluid Dynamics Meeting*, paper 2004-2431, Portland, USA
- [4] Gundersen, T. (2011). Modelling of rotating turbulent flows, Master of science, Norwegian University of Science and Technology
- [5] Huo, C., Barenès, R. and Gressier, J. (2015). Experimental analysis of the aerodynamics of long-shrouded contrarotating rotor in hover, *J. of the American Helicopter Society*, 60 (4)
- [6] Inamuro, T. Lattice Boltzmann methods for moving boundary, *Fluid Dyn. Res.* 44 024001, 2012
- [6] Jardin, T., Prothin, S. and Garcia Magana, C. (2015a). Aerodynamics of micro-rotors in confined environments, 71st Annual Forum of the American Helicopter Society, Virginia Beach, USA
- [7] Jardin, T., Grondin, G. and Gressier, J., Huo, C., Doué, N. and Barènes, R. (2015b). Revisiting Froude's theory for hovering shrouded rotor, *AIAA J.*, 53(7)
- [8] Kalra, T.S., Lakshminarayan, V. K., Baeder, J. and Thomas, S. (2011). Methodological improvements for computational study of hovering micro-rotor in ground effect. 20th AIAA Computational Fluid Dynamics Conference. paper AIAA 2011-3552
- [9] Khromov V and Rand, O. (2008). Ground effect modeling for rotary wing simulation. 26th Congress of International Council of the Aeronautical Sciences. paper ICAS 2008-5.11.3, Anchorage, USA
- [10] Lallemand, P. and Luo, L. S. (2000). Theory of the lattice Boltzmann method: dispersion, dissipation, isotropy, Galilean invariance, and stability, *Phys. Rev. E* 61 (6) 6546-6562
- [11] Lee, T. E., Leishman, J. G., and Ramasamy, M. (2010). Fluid dynamics of interacting blade tip vortices with a ground Plane, *J. of the American Helicopter Society*, 55(2)
- [12] Malaspinas, O. and Sagaut, P. (2012). Consistent subgrid scale modelling for lattice Boltzmann methods. *J. Fluid Mech.*, 700, p. 514-542
- [13] Ota, K., Suzuki, K. and Inamuro, T. (2012). Lift generation by a two-dimensional symmetric flapping wing: immersed boundary Lattice Boltzmann simulations. *Fluid Dyn. Res.*, 44(4)
- [14] Sugiura, M., Tanabe, Y., Sugawara, H., Matayoshi, N. and Ishii, H. (2015). Numerical simulations and measurements of the wake from a helicopter operating in ground effect, 71st Annual Forum of the American Helicopter Society, Virginia Beach, USA
- [15] Wang, M. and Moin, P. (2002). Dynamic wall modeling for large-eddy simulation of complex turbulent flows. *Physics of Fluids*, 14(7)
- [16] Wu, W. and Piomelli, U. (2016). Reynolds-averaged and wall-modelled large-eddy simulations of impinging jets with embedded azimuthal vortices. *European J. of Mechanics – B/Fluids*, 55(2)

